RESEARCH ARTICLE | SEPTEMBER 04 2025

Vertically oriented fiber arrays suppress splashing by restricting spreading of impacting drops *⊗*

Gene Patrick S. Rible ⑩ ; Syed Jaffar Raza ⑩ ; Joshua T. Watkins; Abbey Lin; Visalsaya Chakpuang; Andrew K. Dickerson ➡ ⑩



Physics of Fluids 37, 092106 (2025) https://doi.org/10.1063/5.0286271

A CHORUS





Articles You May Be Interested In

Dynamic drop penetration of vertically oriented fiber arrays

Physics of Fluids (February 2025)

How surface roughness promotes or suppresses drop splash

Physics of Fluids (February 2022)

Reversed role of liquid viscosity on drop splash

Physics of Fluids (May 2021)



Physics of Fluids

Special Topics Open for Submissions

Learn More



ARTICLE

Vertically oriented fiber arrays suppress splashing by restricting spreading of impacting drops

Cite as: Phys. Fluids **37**, 092106 (2025); doi: 10.1063/5.0286271 Submitted: 19 June 2025 · Accepted: 18 August 2025 · Published Online: 4 September 2025







Gene Patrick S. Rible, (D) Syed Jaffar Raza, (D) Joshua T. Watkins, Abbey Lin, Visalsaya Chakpuang, and Andrew K. Dickerson^{a)} (D)

AFFILIATIONS

Department of Mechanical, Aerospace and Biomedical Engineering University of Tennessee, Knoxville, Tennessee 37996, USA

a) Author to whom correspondence should be addressed: dickerson@utk.edu

ABSTRACT

This experimental work builds on our previous studies on the post-impact characteristics of drops striking three-dimensional-printed fiber arrays by investigating the highly transient characteristics of impact. We measure temporal changes in drop penetration depth, lateral spreading, and drop dome height above the fiber array as the drop impacts. Liquid penetration of vertical fibers may be divided into three sequential periods with linearly approximated rates of penetration: (i) an inertial regime, where penetration dynamics are governed by inertia; (ii) a transitional regime exhibiting inertial and capillary action; and (iii) a capillary regime characterized purely by downward wicking. Horizontal fibers exhibit only the inertial and transitional stages, with wicking only observed horizontally along the direction of fibers. In horizontal hydrophilic fiber arrays, the time duration to reach the maximum lateral deformation of the drop is proportional to We^{1/4}, as observed in drops impacting solid surfaces. There exists a critical Weber number below which the drop shows no radial deformation, and the critical value increases with decreasing fiber density. At large Weber numbers, drops splash. In contrast, vertical fibers restrict the lateral spreading of the drop, thereby suppressing a splash for all tested drop velocities, even those exceeding 5 m/s.

Published under an exclusive license by AIP Publishing. https://doi.org/10.1063/5.0286271

I. INTRODUCTION

Vertical fiber arrays play a significant role in various industrial processes. The vertical orientation of the fibers alters the fluid dynamics when the arrays interact with liquids, making them useful in urinal splash suppression, fiber-based coalescers to filter drops contained in mist,² and vertical microfibers that promote rapid nucleation and drop removal to collect water.3 Mechanisms to suppress splashing continue to be an active research area and have numerous existing industrial applications. 4 For instance, certain drainage wearing courses and macrotexture pavements are designed to reduce splash and spray produced by vehicles under wet road conditions, thereby enhancing driver safety. The macro texture of pavements reduces splashing of droplets due to texture,5 thereby increasing road visibility during heavy rainfall. Microtopographic-rough surfaces on hill slopes are employed to create discontinuous ponding and suppress splash entrainment, which helps mitigate soil erosion caused by rain splash and runoff.6 Superhydrophilic coatings investigated for shoe materials have demonstrated virtually no splashing behavior, which can be particularly beneficial in healthcare settings to reduce the transmission of infectious droplets.⁷⁻⁹ Studies have shown that during the decontamination of ultrasound probes, droplets were found on the floor up to 2.2 m away.

Other solutions to minimize splash in such settings include ergonomic workstations, alternative sink designs, and splash barriers. 9

Despite the widespread use of vertical fiber arrays, the mechanisms underlying their ability to suppress splashing have not been extensively investigated in the literature. Drops impacting fiber array structures travel in the direction of the fiber long axis. ¹⁰ Horizontally oriented fiber arrays promote the spread of impacting drops, limiting their penetration depth, ^{11,12} but not necessarily suppressing a splash. Conversely, vertical fibers promote the penetration of impacting drops given sufficient spacing between fibers, while suppressing radial spreading. ¹³ In this work, we investigate how vertical fiber arrays suppress splashing by restricting the radial spread that results in drop disintegration at high Weber numbers. ¹²

Splashing occurs when a liquid drop shatters into smaller daughter droplets at high velocity. ^{14,15} Splashing behavior can be categorized into two types: prompt splash and corona splash. ¹⁶ A prompt splash occurs on rough surfaces, where minor surface roughness disturbances lead to drop formation at the contact line. In contrast, a corona splash occurs on smooth surfaces, where the spreading lamella separates from the substrate, ejecting microscopic drops from its rim due to aerodynamic forces. ^{16,17} Increased surface roughness lowers the splashing

threshold^{18–20} and reduces radial spreading.⁵ In addition to roughness, surface wettability plays a significant role in the splashing behavior of drops.²¹ On solid surfaces, hydrophobicity promotes splashing, as a larger portion of the lamella rises from the surface after the drop reaches maximum spread.^{22,23} At the maximum spread, water and most liquid drops adopt a flat disk or pancake-like shape.^{14,24}

Previous studies have found that a decrease in air pressure, ²⁵ a modification of the microstructure of a surface, ²⁶ and a reduction in pressure around the contact region during drop impact ²⁷ lead to splash suppression. In this work, we again employ our three-dimensional (3D)-printed fiber arrays inspired by mammalian fur, ^{12,13} oriented vertically and cantilevered such that fibers are approximately parallel with each other and gravity. When oriented horizontally, our fiber arrays limit the penetration depth of impacting drops by allowing the drop to spread. ¹² Such a mechanism aids fur in resisting raindrop penetration during a heavy rainfall. In vertical orientations, the restriction in drop spreading lowers the dissipation of kinetic energy, and with the aid of capillarity, drops penetrate deep into the array. ¹³ Here, we focus intently on the suppression of drop breakup during the entry and penetration processes.

II. EXPERIMENTAL SECTION

A. Fur printing, morphology, and wettability

We 3D-print artificial fiber arrays using a FlashForge Hunter Digital Light Processing (DLP) resin printer with a layer resolution of $5 \,\mu \text{m}$ and pixel size of 62.5 μm as done in our previous studies. 12,13 Once cured, the photopolymer resin has a tensile modulus of 48 MPa and a flexural modulus of 2250 MPa. To ensure that the fibers remain aligned during printing, a block of resin anchors the fibers at each end as shown in Fig. 1(a). The structures are printed parallel to the build plate. The fibers are 10 mm long and create a $10 \text{ mm} \times 10 \text{ mm}$ array, ensuring that the drops do not cross the array boundaries during impact. Printer resolution and curing dynamics set a limit on how long and densely packed the fibers can be printed before clumping together into a unified mass. We manufacture fiber arrays at various inter-fiber spacings a (average error on a at 3.8%) in aligned and staggered configurations to produce densities $D \approx 50$, 100, and 150 strands/cm², the higher end being a little greater than that of a gray wolf fur.²⁸ In aligned fiber arrays, the strands repeat in a square array; in staggered fibers, adjacent rows are shifted by a distance of a/2, as shown in Fig. 1(b). Although the fiber alignment affects the drop impact dynamics when the fiber array is horizontally oriented, 12 the radial symmetry of the impacting drop allows staggered and aligned vertical fibers to be functionally equivalent when the fibers are vertical. Each strand is modeled as a square of width $\ell = 350 \, \mu \text{m}$ Fig. 1(b) but gravity during printing causes the resin to flow into a wedge-like shape as shown in Fig. 1(a) so that our fibers have a crosssectional width of $344 \pm 26 \,\mu\text{m}$ (N = 18) and length $394 \pm 50 \,\mu\text{m}$ (N = 18). Such a wedge-like fiber shape appears to be favored in plant leaves and mammalian furs as it promotes water shedding and potentially inhibits penetration. 12,29-3

We perform laser ablation on one end of the fiber array to make the strands cantilevered, after which the samples are coated to be hydrophilic or hydrophobic, ensuring uniform surface wettability. The cured mounting blocks at each fiber terminus, as shown in Fig. 1(a) provide a flat surface on which contact angles are measured as shown in Fig. 1(c). Hydrophobicity of fiber arrays is achieved using vapor phase silanization of the samples with fluorosilane, ^{32,33} resulting in

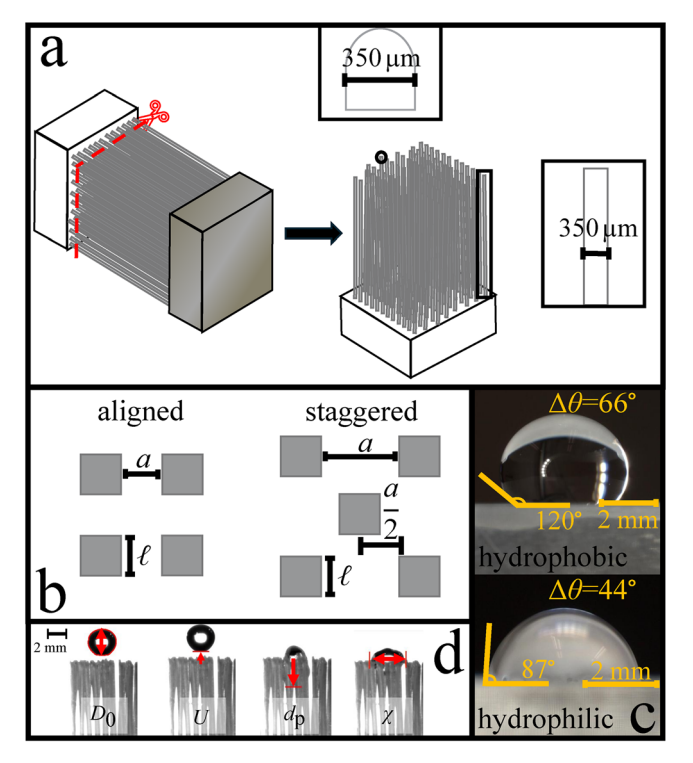


FIG. 1. (a) Fiber arrays are 3D-printed to be affixed on both ends, after which they are laser-ablated on one end; the exposed ends are coated with the rest of the exposed fiber surfaces to even out the surface wettability of the fibers. (b) Aligned and staggered configurations of our vertical fiber arrays. (c) Contact angles of our hydrophilic and hydrophobic fiber arrays. (d) Measurements extracted from the analysis of drop impact videos.

receding, equilibrium, and advancing contact angles of $\theta_r=63\pm9^\circ$ (number of trials, N=3), $\theta_e=120\pm8^\circ$ (N=3), and $\theta_a=129\pm8^\circ$ (N=3), respectively, with contact angle hysteresis $\Delta\theta=\theta_a-\theta_r=66^\circ$. Our hydrophilic fiber array samples are treated with oxygen plasma, leading to the formation of hydroxyl groups on the surface, resulting in contact angles of $\theta_r=68\pm5^\circ$ (N=3), $\theta_e=87\pm1^\circ$ (N=3), and $\theta_a=112\pm6^\circ$ (N=3) with $\Delta\theta=44^\circ$. Since the hydroxyl groups are highly reactive, the contact angles of our hydrophilic samples are bound to increase with time. All trials involving the use of hydrophilic fibers throughout this experiment were completed within two days after the array was prepared.

B. Experimental setup and principal measurements

Drops of fixed diameter of $D_0=2.64\pm0.17~{\rm mm}~(N=111)$ are released from a needle positioned at varying heights of 3, 12, and 24 mm onto a fiber array with impact Reynolds number $Re=\rho UD_0/\mu=376-1980$, where μ is the liquid dynamic viscosity from four heights at corresponding velocities $U=0.21\pm0.04$, 0.37 ± 0.07 , and $0.58\pm0.03~{\rm m/s}$. A fourth height is used to replicate drops with velocities on the lower end of raindrops near 5 m/s. 34,35 To achieve an impact velocity on the order of 5 m/s, drops are released from a known height and allowed to fall under gravity through a vertical guide tube. Vertical guide tubes are widely used to ensure

repeatable and controlled drop impacts. 36-38 The tube serves to isolate the falling drop from ambient air currents. For our impact velocities around 5.5 m/s, the release height is 1.7 m. The actual impact velocities are confirmed using high-speed imaging. The use of the guide tube is critical to the repeatability of our drop impact velocity. For the first three heights, the observed flow of the drop within the fiber array is laminar, so a modified Reynolds number $Re^* = \rho Ua/\mu = 70 - 1025$ that is based on the inter-fiber spacing 12,13,39 better describes the flow of the drops in our fiber arrays. We look at drop impacts on horizontal fibers of similar diameter $D_0 = 2.86 \pm 0.13 \,\mathrm{mm}$ (N = 444) and Reynolds numbers $Re = 730 - 4300 \ (Re^* = \rho Ua/\mu = 100 - 2500)$ for comparison with our vertical impact videos. Our horizontal fiber arrays have the same fiber properties as their vertical counterparts, with drops released from heights 7, 18, 33, and 120 mm above the array. The Ohnesorge Oh is the ratio of the viscous forces to the inertial and surface tension forces during impact and defined as $Oh = \mu / \sqrt{\rho \sigma a}$ where a is the inter-fiber spacing.¹³ The impact Ohnesorge number is $Oh = 2.9 \times 10^{-3} - 5.3 \times 10^{-3}$.

Two synchronized high-speed cameras in front view and oblique view of the fiber array film the drop impact at 3000 fps and a resolution of ≈ 25 px/mm, as shown in Fig. 2. Drop fragmentation is qualitatively observed by the presence of small secondary droplets or fragments that eject with radial or lateral momentum away from the impact site and fiber array, as done in previous works. $^{40-42}$ Based on our recording specifications, the minimum drop fragment that can be recorded would have a diameter $D_0 \approx 0.04$ mm with a maximum speed of ≈ 60 m/s if a drop is moving purely in a horizontal or vertical direction. Drop fragments are $\approx 0.02-0.06$ % of the drop diameter with speeds reaching a maximum of six times the initial velocity. 40 For a typical drop of size $D_0 = 2.64$ mm and velocity U = 5 m/s, we expect fragments to be $\approx 0.05-0.16$ mm and travel at a maximum of 30 m/s. As such, our experimental setup can reliably capture both splashing and fragmentation phenomena.

Between the drop impact trials, the arrays are dried with compressed lab air and never come in contact with human skin. The oblique view camera ensures that the drop impacts within the array bounds. The drop impact video from the front view camera is binarized without inflicting dilation or erosion. From the binarized videos, we track the drop position before impacting the array and measure the

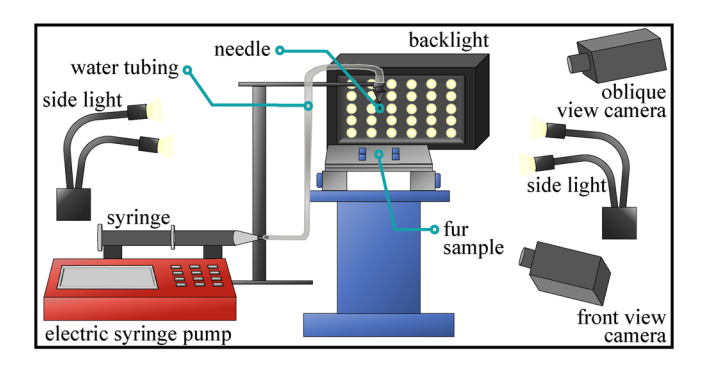


FIG. 2. A drop is dispensed from an electronic syringe pump through a needle, at varying heights, to impact a motionless fiber array. The array is fixed onto a platform with side and backlights illuminating the sample. Front view and oblique view high-speed cameras record the impact.

drop impact velocity U, drop diameter D_0 , penetration depth $d_{\rm p}$, and drop spreading width χ ($\chi=D_0$ pre-impact) as labeled in Fig. 1(d). We nondimensionalize the principal quantities $d_{\rm p}$ and χ , and $d_{\rm h}$ by the drop diameter D_0 to yield

$$\tilde{d}_{\rm p} = d_{\rm p}/D_0$$
, and $\overset{\sim}{\chi} = \chi/D_0$, (1)

and time t by the timescale of impact to yield the dimensionless inertial time $\tau = tU/D_0$. The point at which the drop makes contact is defined as $\tau = 0$.

III. RESULTS AND DISCUSSION

Image sequences of a 3 mm drop impacting a solid surface, a horizontal fiber array, and a vertical fiber array, at the lower end of raindrop speeds \sim 5.32 m/s are shown in Fig. 3 (multimedia available online). On a solid surface shown in Fig. 3(a), the vertical momentum of the drop is abruptly redirected to lateral spreading. The drop immediately splashes upon impact whether the drop reaches the cliff (left) or not (right). On a horizontal fiber array Fig. 3(b), the porosity of the fiber array allows the drop momentum to dissipate more gradually, partially converting some of the momentum to lateral spreading in the process. The drop shatters and splashes immediately upon impact, but there is less splash than on a solid surface. On a vertical fiber array Fig. 3(c), the drop shatters, but the fibers prevent any splashing upon and during impact where fibers are present (left). Where fibers are not present (right) to contain the drop, splashing occurs. If the fibers are made long enough to slow down the drop momentum so that the liquid does not reach the bottom of the fiber array, splashing cannot occur. In Fig. 3(d), we show a high-speed drop impact on an aligned horizontal fiber array side by side with its vertical fiber array counterpart, corresponding to the same elapsed time from the moment of impact. In the vertical fiber array, the right half of the penetrating liquid that is contained within the fiber array does not splash until the bottom is reached when the high velocities cause the drop to splash immediately. Lowering the impact speed of the drop will allow for the investigation of the variables at play before the onset of splashing. Slower impact speeds will allow for the observation of the finer details of the drop impact behavior, such as deformation and spreading that eventually lead to splashing at higher speeds. To investigate the mechanisms for drop splashing and the suppression of splash, we slow down the drop impact velocity to corresponding impact Weber numbers $We = \rho U^2 D_0 / \sigma = 1 - 30$, where ρ is the liquid density and σ is the surface tension of water.

During the impact of drops on vertical fiber arrays, distinct events are observed, as shown in Fig. 4 (multimedia available online). A plot of the spread vs dimensionless time for the drop impact in Fig. 4 is shown in Fig. 5. The first instance of maximum spread, denoted by τ_χ , corresponds to the initial maximal spread. Following the initial maximal spread, the drop recoils or rebounds, leading to a local minimum spread event at $\tau_{(i)}$. Following $\tau_{(i)}$, the drop may experience a local maximum spread at $\tau_{(iii)}$, followed by another local minimum spread, $\tau_{(vii)}$. If the drop reaches the bottom of the array, contact occurs at $\tau_{(iv)}$. Eventually, the drop spread approaches a steady-state value χ_s at $\tau_{\chi,s}$, nondimensionalized as $\chi_s = \chi_s/D_0$. The widest lateral extent achieved by the drop throughout the course of its infiltration within the array is denoted by χ_m , nondimensionalized as $\chi_m = \chi_m/D_0$.



FIG. 4. Image sequence showing the characteristic temporal events in the spreading and penetration of liquid within the array after drop impact. The first instance of maximal spread occurs at τ_χ . As the liquid rebounds, it experiences a minimal spread at $\tau_{(ij)}$. After retraction, the drop spreads out again and reaches a peak at $\tau_{(iij)}$. As the drop continues to infiltrate, the drop reaches the bottom of the fiber array at $\tau_{(iv)}$. The drop spread slightly decreases and reaches a local minimum at $\tau_{(vii)}$ and transitions to a steady-state value at $\tau_{\chi,s}$. The rate of liquid penetration into the array significantly slows down as the impact transitions from the inertial regime to the inertial-capillary regime at $\tau_{(vii)}$. (Multimedia available online).

A. Array penetration

The penetration rate in vertical fiber arrays can be approximated as linear with τ in three different regimes with three distinct slopes, as shown in Fig. 6 (multimedia available online). Grayscale frames are

subtracted from the initial frame, allowing us to see the liquid within the fiber where the human eye falls. Grayscale images are converted to binary and the spread (green), fluid above the fibers (red), and penetration depth (blue) are recorded. The regime with the highest penetration

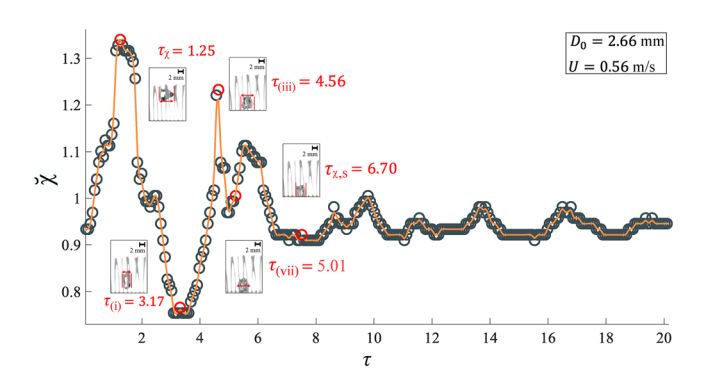


FIG. 5. A plot showing the characteristic temporal events of drop spread when a drop impacts a hydrophilic vertical fiber. The events shown in the graph are the first instance of maximal spread τ_χ , the first instance of minimum spread with rebound $\tau_{(i)}$, the second instance of maximum spread $\tau_{(iii)}$, and the time it takes to achieve steady-state penetration depth $\tau_{\chi,s}$, from left to right.

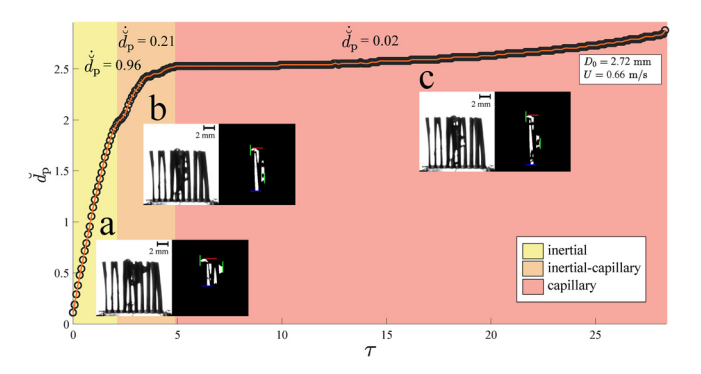


FIG. 6. Three regimes characterizing the penetration behavior of a drop impacting a vertical fiber array. During the (a) inertial regime, penetration is mostly driven by drop momentum with the highest normalized penetration rate of 0.96. As the initial drop momentum dissipates, the normalized penetration rate decreases to 0.23 in the (b) transitional inertial-capillary regime, where penetration is driven by inertia and capillary wicking due to surface tension effects. When all the momentum has dissipated, penetration is driven purely by capillary wicking in the (c) capillary regime at the slowest rate of 0.02. (Multimedia available online).

rate is the inertial regime. The first rate reduction marks the end of the inertial regime, denoted by $\tau_{(ii)}$. A second reduction marks the transition from the inertial-capillary regime to capillary regime, denoted by $\tau_{(y)}$. The inertial regime is parabolic and ends when the drop

penetration rate exhibits non-constant acceleration. ¹³ The capillary regime begins when the drop penetration starts to plateau and the rate of penetration is approximately zero. The average rates of penetration for each regime are recorded as shown in Fig. 6. The deepest penetration achieved in the array is denoted by $d_{\rm p,m}$ and normalized as $d_{\rm p,m} = d_{\rm p,m}/D_0$. Eventually, the drop approaches its steady-state penetration depth $d_{\rm p,s}$ at $\tau_{\rm p,s}$.

The nondimensional rates of penetration or slope of the three regimes in Fig. 6 is $\dot{d}_{\rm p}$, which is equal to the dimensional rates of penetration $\dot{d}_{\rm p}$ nondimensionalized by the drop impact velocity $\dot{d}_{\rm p} = \dot{d}_{\rm p}/U = \Delta \dot{d}_{\rm p}/\Delta \tau$, where $\dot{d}_{\rm p} = \Delta d_{\rm p}/\Delta t$ and t is time in seconds. The rate $\dot{d}_{\rm p}$ for each regime corresponds to the average rate of penetration. The establishment of three penetration regimes allows us to investigate the spreading of drops within the context of the penetration behavior, which has been shown to directly influence spreading. 12

Effects due to fiber geometry are likely to dominate in the inertial-capillary and capillary regimes, where surface roughness and wettability play roles in contact line recession. In contrast, we believe that the cross section geometry has minimal effects in the inertial regime, which is the primary site of splashing and the dominant transport mechanism shown in Fig. 6. Thus, we suspect fiber geometry to have a minimal influence on the inhibition dynamics of splashing in vertical fibers. Since the cross section is held constant for all experiments, its influence in successive trials is not important, and our comparative results are not influenced. We anticipate that future studies using different cross-sectional shapes, such as the symmetric circular or square vs our asymmetric wedge-shaped fibers of similar scale, could reveal variations in final penetration depth and lateral spreading, particularly in sufficiently large fiber arrays. Additionally, larger or smaller cross sections could further modulate capillary pressure and fluid transport pathways.

Vertical drops, on occasion, fully penetrate the fiber array and hit the fiber baseplate, and when impacting with sufficient speed, cause the drops to splash. The occurrence of such an event depends on the inertial properties driving the penetration of the drop relative to the viscous forces halting the drop: the fiber density and the fiber length. We define a dimensionless value $\Omega = D_0 Re/(OhL)$ that can be used to set the threshold value for full penetration within a fiber array of depth L. We plot the maximum penetration depth nondimensionalized by the fiber array length $d_{\rm p,m}/L$ vs Ω for our hydrophilic and hydrophobic vertical fiber arrays in Fig. 7. A value of $d_{\rm p,m}/L \approx 1$

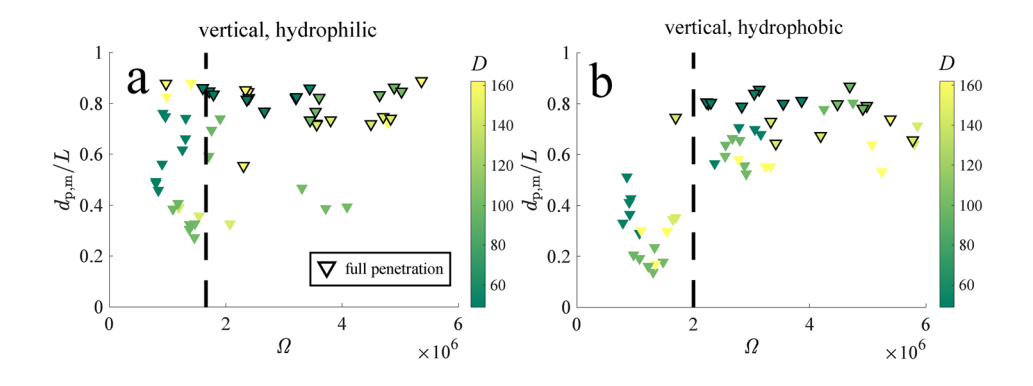


FIG. 7. Plot of the maximum penetration depth normalized by recorded fiber length $d_{\mathrm{p,m}}/L$ vs Ω for (a) hydrophilic and (b) hydrophobic vertical fibers. Outlined data points indicate full penetration, the liquid reaching the bottom of the fiber array.

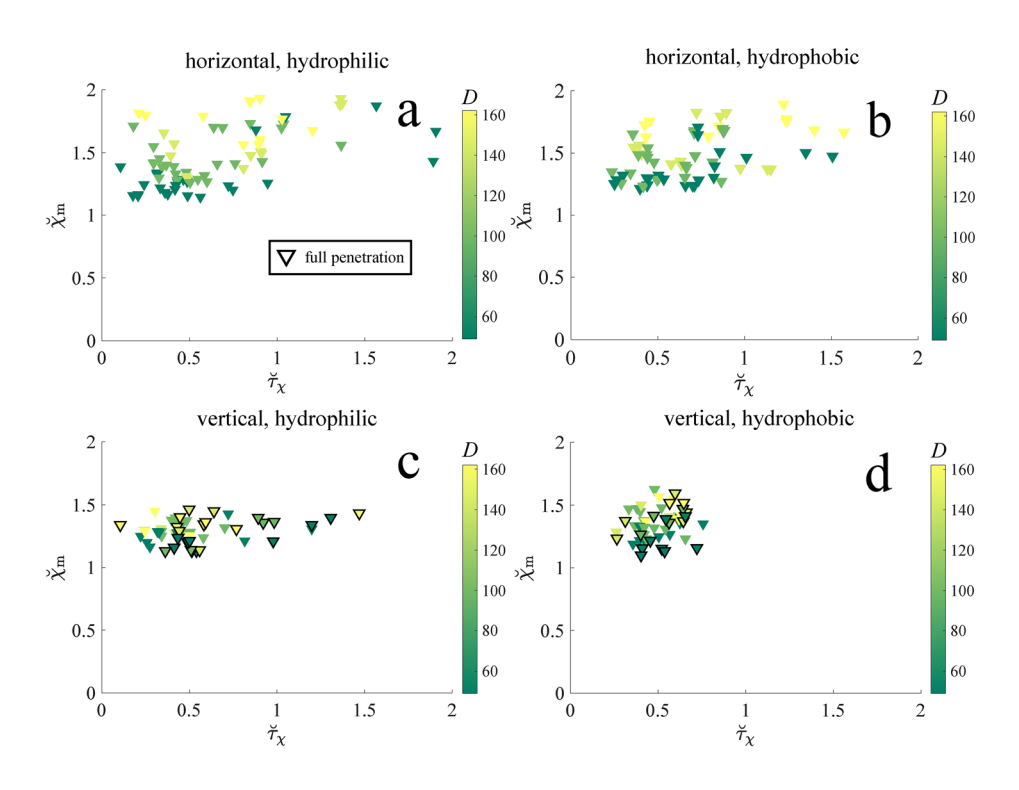


FIG. 8. Plot of steady-state spread vs the first instance of maximal spread τ_χ in (a) and (b) horizontal and (c) and (d) vertical fiber arrays. Plots on the left column correspond to hydrophilic fibers, whereas plots on the right column correspond to hydrophobic fibers. Outlined data points indicate full penetration, the liquid reaching the bottom of the array. Fiber density D of our arrays sets the gradient bar on the right of each plot. Brighter yellow tones indicate denser fiber arrays.

implies full penetration, indicated by the data points with a black outline. We set L=10 mm but because our fiber arrays are laser-ablated on one end, the actual length L is reduced so that $d_{\rm p,m}/L\approx 0.8$ already indicates full penetration as shown in Fig. 7. The threshold value after

which infiltration occurs is $\Omega \approx 1.75 \times 10^6$ for our hydrophilic and $\Omega \approx 2 \times 10^6$ for our hydrophobic fiber arrays. The threshold value corresponds to an approximate value of Ω , which is identified as the dividing point between most of the complete and incomplete

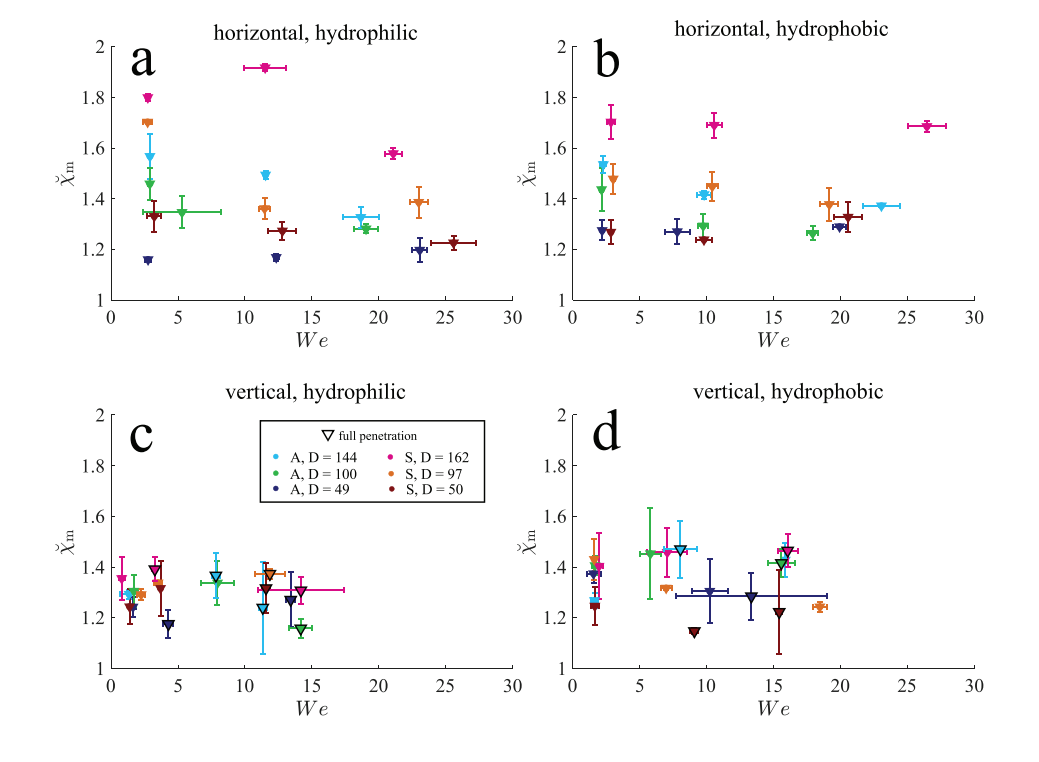


FIG. 9. Plot of nondimensional maximum spread vs Weber number for (a-b) horizontal and (c-d) vertical fibers in aligned (A) and staggered (S) configurations. Fiber density D is in cm⁻². Outlined data points indicate full penetration, the liquid reaching the bottom of the fiber array.

penetration events in our vertical fiber arrays. However, these are not exact values and serve as a practical guideline rather than a strict physical boundary. While we do not test a range of speeds and drop properties, the formation of a group that predicts a nearly certain splash is useful for designing vertical fiber arrays that ensure the complete suppression of a splash.

B. Splash suppression by spread restriction

Given sufficient fiber length and the range of experimental D that we test, we posit that drops will not splash entering vertical fibers for terminal raindrop speeds. The experimental absence of splashing for impacts that do not consume the entire fiber length suggests that the preferred direction of travel of the drop within the array is critical for suppressing breakup. We thus examine how little drops spread laterally in such arrays. We plot $\chi_{\rm m}$ vs τ_{χ} for horizontal and vertical fiber arrays in Fig. 8. The brighter yellow tones indicate a higher fiber density. The plots reveal a positive correlation between the maximum spread $\chi_{\rm m}$ achieved by the penetrating liquid and the time it takes to reach the first instance of maximum spread τ_{γ} . The range of τ_{χ} is

greater for horizontal fibers (0–2) than for vertical fibers (0–1) and as expected, greater for hydrophilic fiber arrays than their hydrophobic counterparts since hydrophobic fibers allow the liquid contact line to recede. ¹² The vertical orientation of the fibers constrains the direction of travel of the drop, restricting spread and consequently suppressing splash.

Hydrophobic fiber arrays demonstrate greater restriction of lateral spreading compared with their hydrophilic counterparts. Nevertheless, we observe complete splash suppression in all vertical fiber array configurations, even at impact velocities exceeding 5 m/s. In contrast, splashing consistently occurs in both hydrophilic and hydrophobic horizontal fiber arrays at these higher velocities. These results highlight that fiber orientation, rather than surface wettability alone, is the dominant factor governing splash suppression. Suppression of splash is not expected to be a property of non-draining arrays with repeated drop impacts. Arrays that foul with solids or fill with liquid will promote splashing as the array begins to resemble a rough surface 41–44 or a pooled surface, 45 respectively.

Upon impact on vertical fiber arrays, the initial spreading of the lamella is significantly hindered due to early contact with multiple

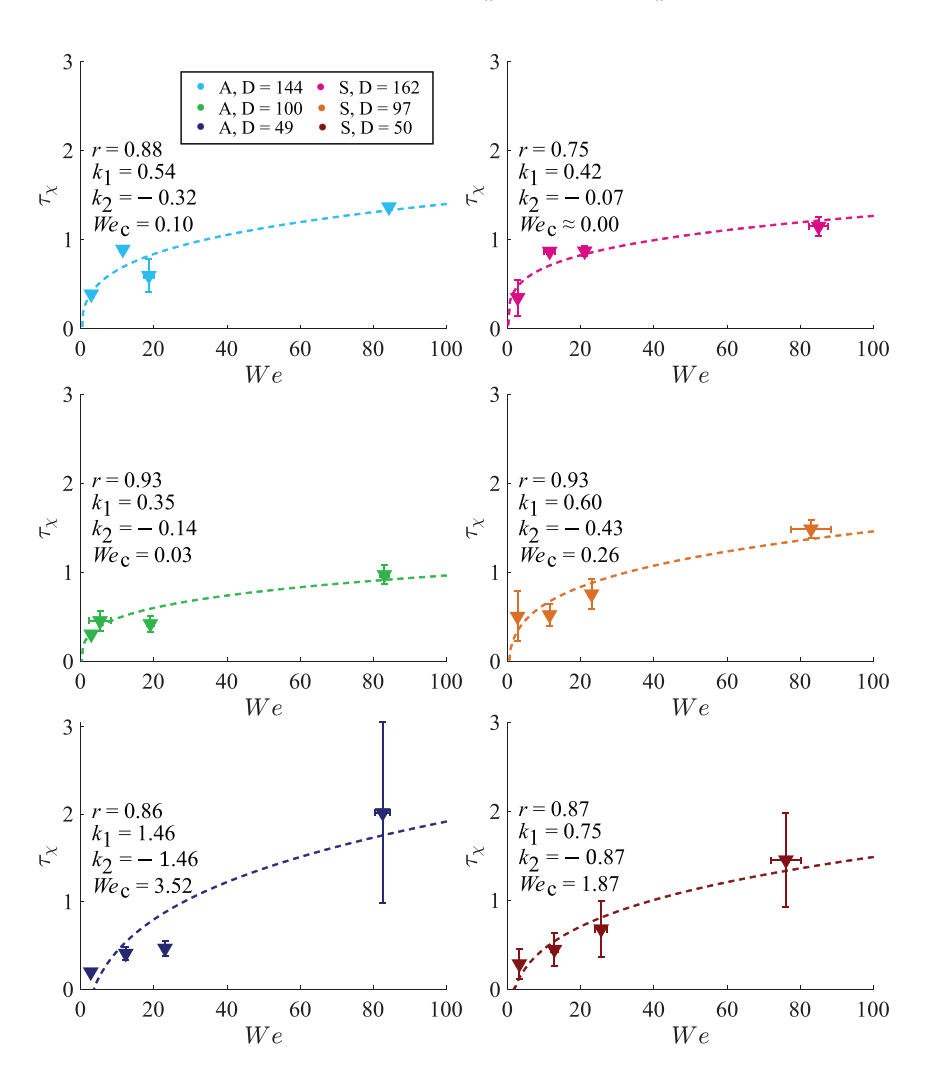


FIG. 10. Plot of the first instance of local maximum spread vs the Weber number for hydrophilic horizontal fibers in aligned (A) and staggered (S) configurations. Fiber density D is in cm $^{-2}$. At a critical number We_c , the drop experiences no radial deformation upon and after impact. The model coefficients are given by k_1 and k_2 , refer to Eq. (2). The absolute value of the Pearson correlation coefficient |r| = 0 - 1 indicates the fidelity of the model to the actual data points, with a value of 1 indicating a perfect fit. A negative r indicates a wrong fit.

upright fiber elements. Such geometric obstruction redirects and redistributes the radial momentum of the spreading liquid, effectively truncating the lamella before it can form a thin, fast-moving sheet, an essential precursor to lift-up and rim instability. 40,46,47 By constraining the radial expansion and introducing vertical flow components along the fibers, the system diminishes the kinetic conditions necessary for lamella lift-off.46 The altered flow path and energy dissipation into the vertical structure appear to limit the ability of the rim to detach from the substrate, a key requirement for the onset of instabilities like the Plateau-Rayleigh breakup or aerodynamic entrainment. 48-50 Our high-speed visualizations indicate that the primary suppression occurs at earlier stages before rim formation and instability mechanisms can fully develop. Vertical fiber arrays introduce a significantly stronger form of three-dimensional confinement, particularly in the radial direction. In contrast, horizontal fiber arrays primarily constrain vertical motion but still allow considerable in-plane radial expansion across the top layer. As such, horizontal fiber arrays provide partial confinement, insufficient to disrupt the lamella formation and spreading dynamics that lead to splashing.

In horizontal fibers, spreading is promoted, thereby reducing penetration depth and allowing for splashing at higher 12 We. As fiber density increases, the spreading of the liquid in horizontal and vertical fibers increases. The maximum liquid spreading χ m achieved within the array is plotted against We in Fig. 9. Maximum spreading is restricted in vertical fibers, with a mean reduction of 6.8% and 2.0% in χ m across comparable drop levels for hydrophilic and hydrophobic fiber arrays, respectively, with select densities and levels reaching up to 27.0% (hydrophilic, $162 \, \mathrm{cm}^{-2}$) and 29% (hydrophobic, $50 \, \mathrm{cm}^{-2}$) reduction in vertical fiber arrays compared with their horizontal counterparts, as shown in Fig. 9. In horizontal fibers, denser fibers promote spreading. In vertical fibers, spreading is independent of fiber density. In the limit of increasing fiber density, a vertical fiber array acts as a rough solid surface, which has been shown to facilitate splashing.

The first instance of local maximum spread is plotted against the Weber number for horizontal fibers in Figs. 10 and 11 and for vertical fibers in Figs. 12 and 13. Each subplot contains 9–12 experimental data points. While it may appear that only 3–4 data points are shown, each plotted point represents the average of three independent

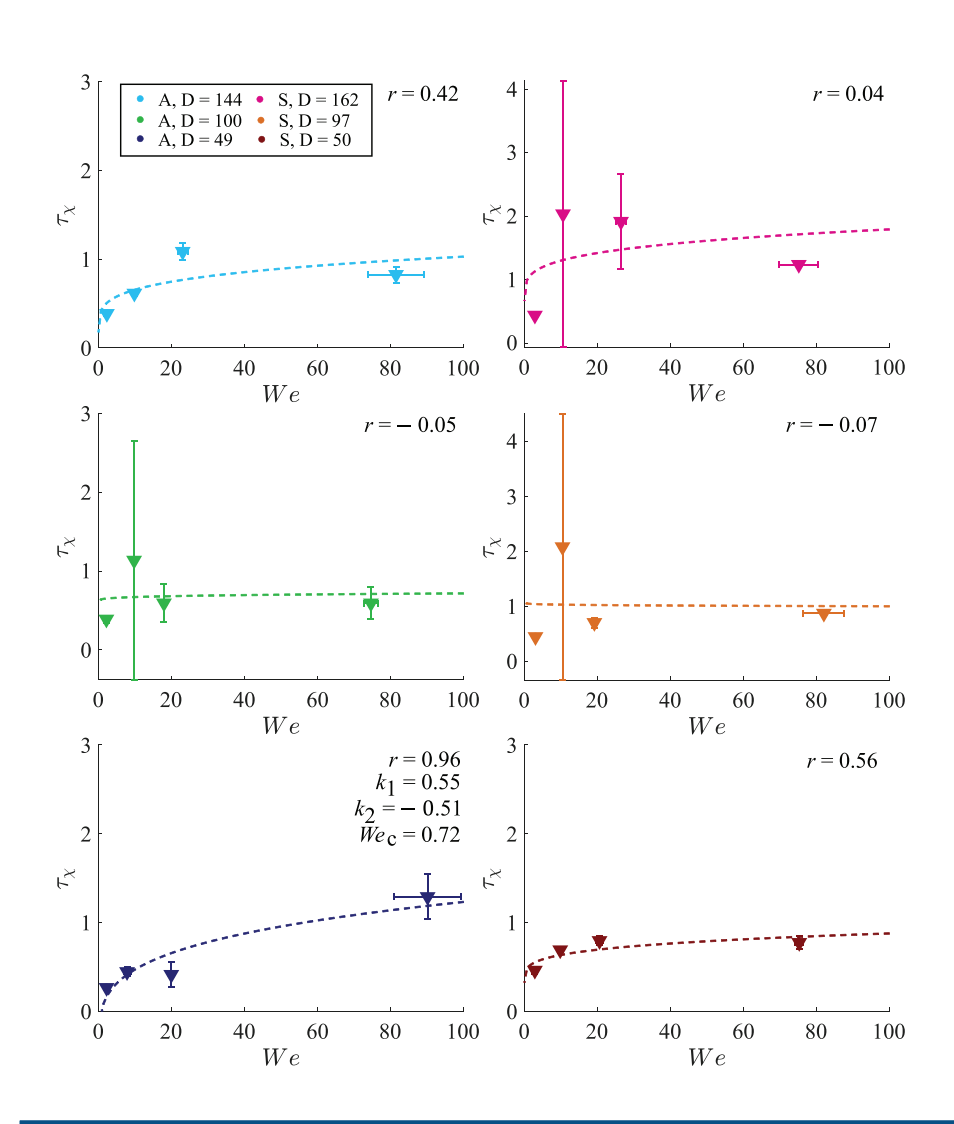


FIG. 11. Plot of the first instance of local maximum spread vs the Weber number for hydrophobic horizontal fibers in aligned (A) and staggered (S) configurations. Fiber density D is in cm $^{-2}$. A critical number We_c only exists ($We_c \ge 0$) for one fiber type where We_c is specified. The absolute value of the Pearson correlation coefficient |r| = 0 - 1 indicates the fidelity of the model to the actual data points, with a value of 1 indicating a perfect fit. A negative r indicates a wrong fit.

measurements at the same condition, for a total of 9–12 individual data points per subplot. The first instance of local maximum spread τ_χ is positively correlated with We in horizontal fibers. In vertical fibers where spreading is restricted, τ_χ is independent of We, especially at higher densities. The time to reach the first instance of maximum spreading for a drop impacting a solid surface has previously been shown to be proportional to Ref. 51 $We^{1/4}$. We observe the same relationship in our fiber arrays,

$$\tau_{\gamma} = k_1 W e^{1/4} + k_2, \tag{2}$$

where k_1 and k_2 are constants, as shown in Fig. 10.

Furthermore, in hydrophilic horizontal fiber arrays, there exists a critical Weber number We_c at which no radial deformation occurs at all fiber densities. In practice, slight deformation may still occur due to mechanical interactions between the drop and the fiber array. Nonetheless, lateral spreading remains minimal at or below the identified We_c , validating its role as a useful transition criterion between spreading and non-spreading behavior. In cases where the $We_c < 1$, it is impossible to produce drops using a needle as the minimum pinch

off velocity of 3 mm drops is $U=0.155\,\mathrm{m/s}$, which corresponds to a Weber number $We=1.^{52,53}$

The critical Weber number in hydrophobic horizontal fibers cannot be obtained (i.e., $We_c < 0$, which is not possible) from the model in Eq. (2) as shown in Fig. 11. Hydrophobic horizontal fibers have increased fluctuation in spreading events and less dependence on We, which is evidenced by the latency of spreading events. The latency from the first instance of maximum spread to the time of steady-state spread $\Delta \tau = \tau_{\gamma,s} - \tau_{\gamma}$ is shown in Fig. 14. Latency in hydrophilic horizontal fibers increases with We, as shown in Fig. 14(a), whereas the latency is independent of We in hydrophobic horizontal fibers, as shown in Fig. 14(b). We attribute the variation in spread events to the persistent advance and recession of the contact line after a drop impacts our horizontal arrays. Such a back-and-forth motion renders time events less stable and results in poor correlation with $We^{1/4}$, as shown in Fig. 11. Higher densities approach a rough porous surface and have worse correlation coefficients. As We increases past a threshold value in horizontal fibers, splashing occurs as shown in Fig. 3(b) the transition from spreading to splashing past a critical We has been observed in solid and rough surfaces.4

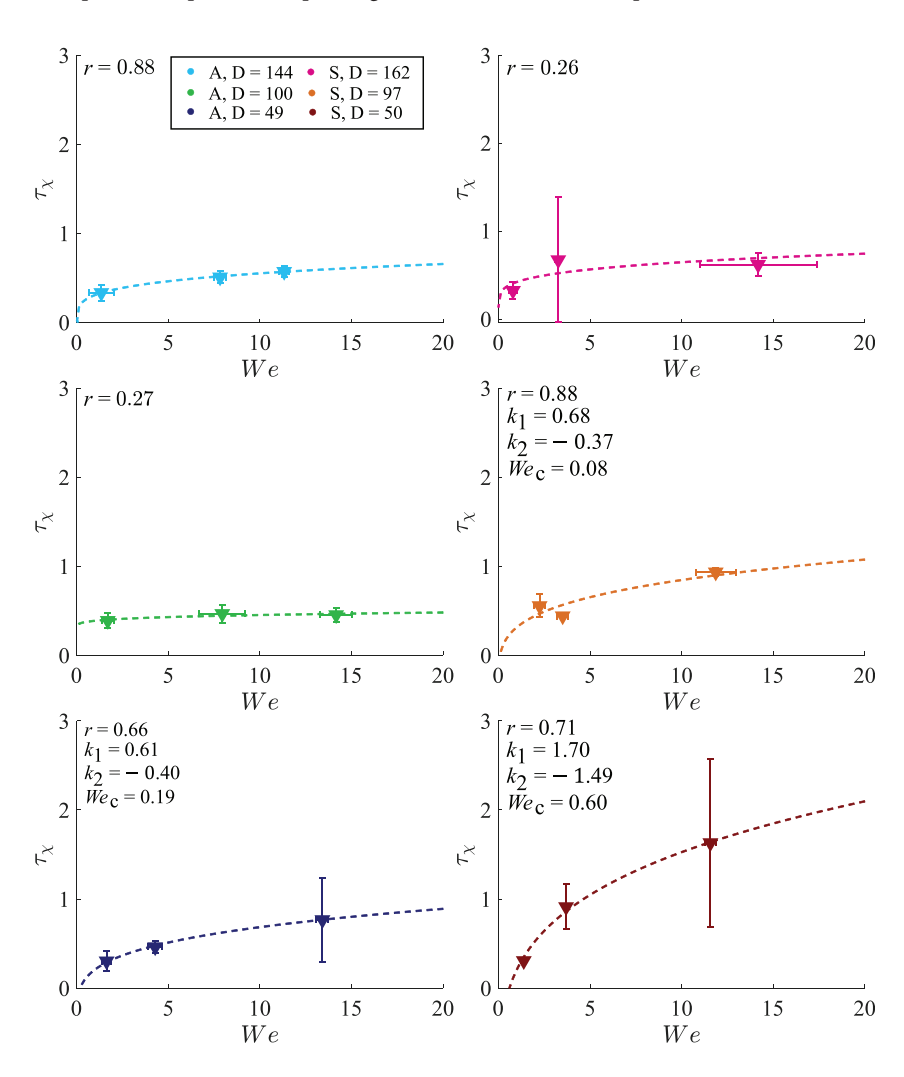


FIG. 12. Plot of the first instance of local maximum spread vs the Weber number for hydrophilic vertical fibers in aligned (A) and staggered (S) configurations. Fiber density D is in cm $^{-2}$. A critical number $We_{\rm c}$ only exists $(We_{\rm c} \geq 0)$ for certain fiber types where $We_{\rm c}$ is specified. The absolute value of the Pearson correlation coefficient |r|=0-1 indicates the fidelity of the model to the actual data points, with a value of 1 indicating a perfect fit. A negative r indicates a wrong fit.

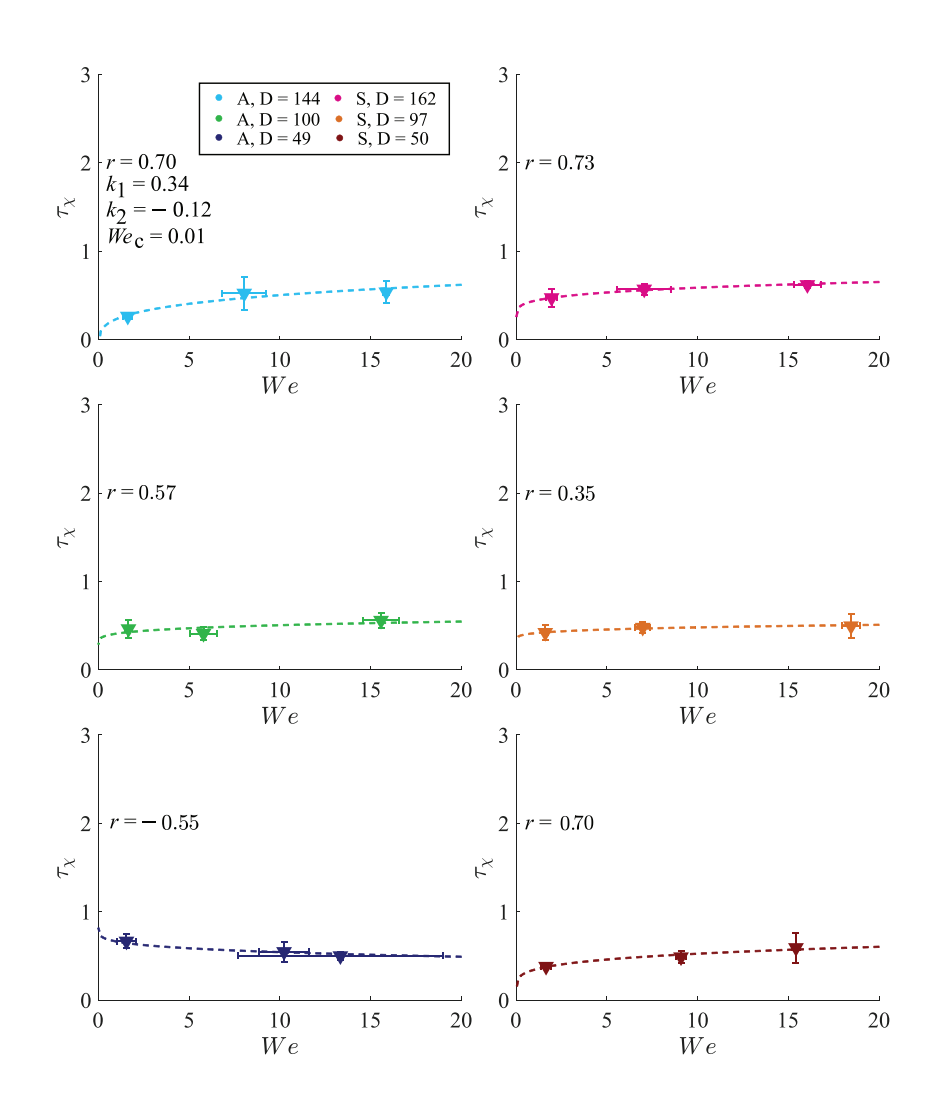


FIG. 13. Plot of the first instance of local maximum spread vs the Weber number for hydrophobic vertical fibers in aligned (A) and staggered (S) configurations. Fiber density D is in cm $^{-2}$. A critical number $We_{\rm c}$ only exists $(We_{\rm c} \geq 0)$ for certain fiber types where $We_{\rm c}$ is specified. The absolute value of the Pearson correlation coefficient |r|=0-1 indicates the fidelity of the model to the actual data points, with a value of 1 indicating a perfect fit. A negative r indicates a wrong fit.

 $We_{\rm c}$ does not exist for higher densities in vertical hydrophilic fibers, as shown in Fig. 12, as increased density when the fibers are vertically oriented will make the vertical fiber arrays resemble rough porous solid surfaces, which are known to induce splashing of impacting drops. 42,54 As in horizontal fibers, hydrophobic vertical fibers lack dependence on We, as shown in Fig. 13. Latency in hydrophilic vertical fibers increases with We, as shown in Fig. 14(c), whereas the latency is independent of We in hydrophobic vertical fibers, as shown in Fig. 14(d). We attribute the variation in spread events in vertical fibers to the lack of contact line pinning. 12 In the vertical fiber arrays that we tested, splashing is completely suppressed for all tested drop velocities, including those exceeding 5 m/s, which is at the lower end of raindrop velocities. 34,35

Drops falling onto geometries with limited surface area tend to splash downward, even during fragmentation on contact.⁵⁵ If provided a wide array of these geometries, such as in our vertical fiber arrays, then contact with each fiber would dissipate kinetic energy⁴⁰ while containing the spreading liquid. Provided a sufficiently wide and long fiber array, we suspect complete suppression of splash even upon fragmentation on contact, as all the liquid will be contained in the array.

IV. CONCLUSION

In this paper, we establish that drops impacting vertical fibers exhibit restricted spread, leading to suppressed splash behavior. The first instance of maximal spread is achieved faster in vertical fibers compared with horizontal fibers, indicating enhanced spread restriction in vertical fibers. The time to achieve the first instance of maximum spread from the moment of impact is proportional to $We^{1/4}$ in horizontal and vertical fiber arrays with stronger correlations in hydrophilic fibers as opposed to hydrophobic. The latency from the first instance of maximum spread to the time of steady-state spread increases with We in hydrophilic fibers, but the correlation becomes poorer in hydrophobic fibers. We attribute the variation in spread events to the persistent advance and recession of the contact line after a drop impacts our hydrophobic fiber arrays. Such a back-and-forth motion renders time events less stable and results in poor correlation with We. The first instance of maximal spread is expedited by hydrophobicity and independent of fiber density in both horizontal and vertical fiber arrays. Vertical fibers exhibit three drop penetration regimes: inertial, transitional, and capillary. No splashing behavior is observed in our vertical fibers for all tested velocities up to approximately 5 m/s,

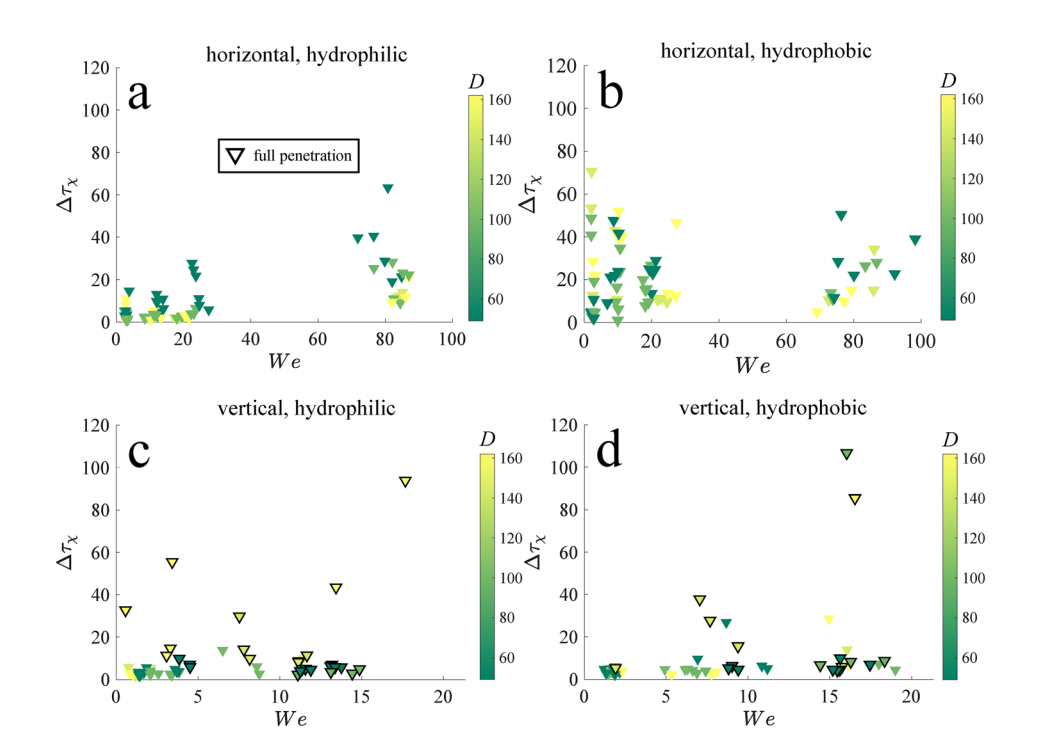


FIG. 14. Plot of the latency from the first instance of maximum spread to the time of steady-state spread $\Delta\tau=\tau_{\chi,s}-\tau_{\chi}$ vs the Weber number We for (a) and (b) horizontal and (c) and (d) vertical fibers in aligned (A) and staggered (S) configurations. Fiber density D is in cm $^{-2}$. Outlined data points indicate full penetration, the liquid reaching the bottom of the fiber array.

which is at the lower end of raindrop velocities. To characterize the likelihood of penetrated liquid reaching the bottom of a vertical fiber array after impact, we propose a nondimensional group that incorporates fiber length, drop diameter, and impact velocity and scales as the ratio of the Reynolds number to the Ohnesorge number. When a penetrating liquid with sufficient momentum collides with the bottom surface of a vertical fiber array, splashing occurs.

ACKNOWLEDGMENTS

This research was partially funded by the National Science Foundation (CMMI 1825801 and CBET 2205558). We thank undergraduate research assistants at the Fluids and Structures Laboratory, Hadi Bhidya for bespoke code and video analysis contributions, and Aaron Matheny for performing drop impact experiments at raindrop velocities.

AUTHOR DECLARATIONS Conflict of Interest

The authors have no conflicts to disclose.

Author Contributions

Gene Patrick S. Rible: Conceptualization (lead); Data curation (supporting); Formal analysis (supporting); Investigation (lead); Methodology (lead); Project administration (lead); Resources (lead); Software (supporting); Supervision (lead); Validation (equal); Visualization (equal); Writing – original draft (supporting); Writing – review & editing (lead). Syed Jaffar Raza: Conceptualization (equal); Data curation (lead); Formal analysis (lead); Investigation (equal); Methodology (equal); Project administration (equal); Software (lead);

Supervision (equal); Validation (equal); Visualization (lead); Writing – original draft (supporting). **Joshua T. Watkins:** Data curation (equal); Formal analysis (equal); Investigation (equal); Methodology (equal); Software (equal); Supervision (equal); Validation (equal); Visualization (equal). **Abbey Lin:** Investigation (supporting); Validation (supporting); Visualization (supporting); Writing – original draft (lead); Writing – review & editing (equal). **Visalsaya Chakpuang:** Data curation (equal); Formal analysis (supporting); Investigation (supporting); Methodology (supporting); Software (equal). **Andrew K. Dickerson:** Conceptualization (equal); Funding acquisition (lead); Resources (equal); Validation (equal); Writing – original draft (equal); Writing – review & editing (equal).

DATA AVAILABILITY

The data that support the findings of this study are available from the corresponding author upon reasonable request.

REFERENCES

- ¹A. M. Nasto, "Hairy interfaces," Ph.D. thesis (Massachusetts Institute of Technology, 2018).
- ²A. Schwarzwälder, J. Meyer, and A. Dittler, "Experimental analysis of droplet coalescence and transport mechanisms on a single vertical fiber," Exp. Fluids 64, 103 (2023).
- ³X. Wang, X. Zhou, N. Luo, H. Luo, H. Wei, B. Qin, J. Zeng, X. Yu, Y. Mei, and Y. Zhang, "Beetle-like structured microfibers for rapid water harvesting," Appl. Surf. Sci. 638, 158090 (2023).
- ⁴F. Pérez-Jiménez, A. Martínez, F. Sánchez-Domínguez, and J. A. Ramos-García, "System for measuring splash on wet pavements," Transp. Res. Rec. 2227, 171 (2011).
- ⁵R. K. Singh, P. D. Hodgson, N. Sen, and S. Das, "Effect of surface roughness on hydrodynamic characteristics of an impinging droplet," Langmuir 37, 3038 (2021).

- ⁶R. B. Bryan, "Soil erodibility and processes of water erosion on hillslope," Geomorphology 32, 385 (2000).
- ⁷P. Aranega-Bou, C. Cornbill, N. Verlander, and G. Moore, "A splash-reducing clinical handwash basin reduces droplet-mediated dispersal from a sink contaminated with Gram-negative bacteria in a laboratory model system," J. Hosp. Infect. 114, 171 (2021).
- ⁸R. Mathew, R. Mohindra, A. Sahu, R. Bhat, A. Ramaswami, and P. Aggarwal, "Occupational sharp injury and splash exposure among healthcare workers in a tertiary hospital," J. Lab. Phys. 13, 323 (2021).
- ⁹C. L. Ofstead, K. M. Hopkins, F. E. Daniels, A. G. Smart, and H. P. Wetzler, "Splash generation and droplet dispersal in a well-designed, centralized high-level disinfection unit," Am. J. Infection Control 50, 1200 (2022).
- ¹⁰K. Picha, C. Spackman, and J. Samuel, "Droplet spreading characteristics observed during 3D printing of aligned fiber-reinforced soft composites," Addit. Manuf. 12, 121 (2016).
- ¹¹J. Zheng, J. Wang, Y. Yu, and T. Chen, "Hydrodynamics of droplet impingement on a thin horizontal wire," Math. Probl. Eng. 2018, 1.
- ¹²G. P. S. Rible, M. A. Spinazzola III, R. E. Jones III, R. U. Constantin, W. Wang, and A. K. Dickerson, "Dynamic drop penetration of horizontally oriented fiber arrays," Langmuir 40, 13339 (2024).
- ¹³G. P. S. Rible, V. Chakpuang, A. D. Holihan, H. P. Sebek, H. H. Osman, K. R. Brown, W. Wang, and A. K. Dickerson, "Dynamic drop penetration of vertically oriented fiber arrays," Phys. Fluids 37, 022108 (2025).
- ¹⁴G. Liang, Y. Chen, L. Chen, and S. Shen, "Maximum spreading for liquid drop impacting on solid surface," Ind. Eng. Chem. Res. 58, 10053 (2019).
- 15J. Liu, H. Vu, S. S. Yoon, R. A. Jepsen, and G. Aguilar, "Splashing phenomena during liquid droplet impact," Atomization Sprays 20, 297 (2010).
- 16 H. Zhang, X. Zhang, X. Yi, Y. Du, F. He, F. Niu, and P. Hao, "How surface roughness promotes or suppresses drop splash," Phys. Fluids 34, 022111 (2022).
- ¹⁷L. Xu, "Liquid drop splashing on smooth, rough, and textured surfaces," Phys. Rev. E 75, 056316 (2007).
- ¹⁸F. R. Smith, N. C. Buntsma, and D. Brutin, "Roughness influence on human blood drop spreading and splashing," <u>Langmuir</u> 34, 1143 (2018).
- ¹⁹Q. Wang, X. Lin, Y. Lin, J. Ma, J. Xiao, Y. Wu, and J. Wang, "Effects of surface roughness on splashing characteristics of large droplets with digital inline holographic imaging," Cold Reg. Sci. Technol. 191, 103373 (2021).
 ²⁰Y.-Y. Zhuo, S. Hussain, and S.-Y. Lin, "Effect of surface roughness on the collision
- ²⁰Y.-Y. Zhuo, S. Hussain, and S.-Y. Lin, "Effect of surface roughness on the collisior dynamics of water drops on wood," Colloids Surf., A 612, 125989 (2021).
- H. Almohammadi and A. Amirfazli, "Droplet impact: Viscosity and wettability effects on splashing," J. Colloid Interface Sci. 553, 22 (2019).
 H. Almohammadi and A. Amirfazli, "Understanding the drop impact on mov-
- ing hydrophilic and hydrophobic surfaces," Soft Matter 13, 2040 (2017).

 23D. C. Aboud and A. M. Victoig, "Spleshing threshold of oblique drople
- ²³D. G. Aboud and A.-M. Kietzig, "Splashing threshold of oblique droplet impacts on surfaces of various wettability," Langmuir 31, 10100 (2015).
- ²⁴J. B. Lee, N. Laan, K. G. de Bruin, G. Skantzaris, N. Shahidzadeh, D. Derome, J. Carmeliet, and D. Bonn, "Universal rescaling of drop impact on smooth and rough surfaces," J. Fluid Mech. 786, R4 (2016).
- ²⁵A. Latka, A. Strandburg-Peshkin, M. M. Driscoll, C. S. Stevens, and S. R. Nagel, "Creation of prompt and thin-sheet splashing by varying surface roughness or increasing air pressure," Phys. Rev. Lett. 109, 054501 (2012).
- ²⁶Y. Liu, P. Tan, and L. Xu, "Kelvin-Helmholtz instability in an ultrathin air film causes drop splashing on smooth surfaces," Proc. Natl. Acad. Sci. USA 112, 3280 (2015).
- ²⁷C. J. Howland, A. Antkowiak, J. R. Castrejón-Pita, S. D. Howison, J. M. Oliver, R. W. Style, and A. A. Castrejón-Pita, "It's harder to splash on soft solids," Phys. Rev. Lett. 117, 184502 (2016).
- ²⁸M. W. Kulbaba, "Investigating epizoochorous adaptations to mammalian furs," Ph.D. thesis (Department of Biology, University of Winnipeg, 2004).
- ²⁹A. P. Lebanoff and A. K. Dickerson, "Drop impact onto pine needle fibers with non-circular cross section," Phys. Fluids 32, 092113 (2020).
- ³⁰M. Krsmanovic, D. Biswas, H. Ali, A. Kumar, R. Ghosh, and A. K. Dickerson, "Hydrodynamics and surface properties influence biofilm proliferation," Adv. Colloid Interface Sci. 288, 102336 (2021).

- ³¹M. Krsmanovic, R. Ghosh, and A. K. Dickerson, "Fur flutter in fluid flow fends off foulers," J. R. Soc. Interface 20, 20230485 (2023).
- ³²W. Wang, X. Du, H. Vahabi, S. Zhao, Y. Yin, A. K. Kota, and T. Tong, "Trade-off in membrane distillation with monolithic omniphobic membranes," Nat. Commun. 10, 3220 (2019).
- 33W. Wang, J. Salazar, H. Vahabi, A. Joshi-Imre, W. E. Voit, and A. K. Kota, "Metamorphic superomniphobic surfaces," Adv. Mater. 29, 1700295 (2017).
- ³⁴R. Gunn and G. D. Kinzer, "The terminal velocity of fall for water droplets in stagnant air," J. Meteor. 6, 243 (1949).
- 35V. Bringi, M. Thurai, and D. Baumgardner, "Raindrop fall velocities from an optical array probe and 2-D video disdrometer," Atmos. Meas. Tech. 11, 1377 (2018).
- ³⁶G. Jurez, T. Gastopoulos, Y. Zhang, M. L. Siegel, and P. E. Arratia, "Splash control of drop impacts with geometric targets," Phys. Rev. E 85, 026319 (2012).
- 37J. Parmentier, V. Terrapon, and T. Gilet, "Drop impact on thin film: Mixing, thickness variations, and ejections," Phys. Rev. Fluids 8, 053603 (2023).
- ³⁸I. Dimino, G. Diodati, F. Di Caprio, M. Ciminello, A. Menichino, M. Inverno, M. Belardo, and L. Di Palma, "Numerical and experimental studies of free-fall drop impact tests using strain gauge, piezoceramic, and fiber optic sensors," Appl. Mech. 3, 313 (2022).
- ³⁹P. J. Pritchard and J. W. Mitchell, Fox and McDonald's Introduction to Fluid Mechanics (John Wiley & Sons, 2016).
- ⁴⁰D. A. Burzynski, I. V. Roisman, and S. E. Bansmer, "On the splashing of high-speed drops impacting a dry surface," J. Fluid Mech. 892, A2 (2020).
- ⁴¹N. P. Sapkal, S. C. Park, Y. W. Lee, and D. I. Yu, "Experimental study of droplet splashing phenomena on hydrophobic micro-and micro/nano-textured surfaces," J. Mech. Sci. Technol. 35, 5061 (2021).
- ⁴²J. Hao, "Effect of surface roughness on droplet splashing," Phys. Fluids 29, 122105 (2017).
- ⁴³M. A. Quetzeri-Santiago, A. A. Castrejón-Pita, and J. R. Castrejón-Pita, "The effect of surface roughness on the contact line and splashing dynamics of impacting droplets," Sci. Rep. 9, 15030 (2019).
- ⁴⁴H. Kim, U. Park, C. Lee, H. Kim, M. Hwan Kim, and J. Kim, "Drop splashing on a rough surface: How surface morphology affects splashing threshold," Appl. Phys. Lett. **104**, 161608 (2014).
- 45 M. Artman-Breitung, D. A. Watson, and A. K. Dickerson, "Simultaneous impact of twin drops on a semi-infinite liquid target," Phys. Fluids 33, 102110 (2021).
- ⁴⁶K. Cardin, C. Josserand, and R. B. Cal, "Droplet capture in a fiber array," Phys. Rev. Fluids 8, 043601 (2023).
- ⁴⁷C. Tang, M. Qin, X. Weng, X. Zhang, P. Zhang, J. Li, and Z. Huang, "Dynamics of droplet impact on solid surface with different roughness," Int. J. Multiphase Flow 96, 56 (2017).
- ⁴⁸I. M. Jackiw and N. Ashgriz, "Prediction of the droplet size distribution in aerodynamic droplet breakup." J. Fluid Mach. 940, A17 (2022)
- dynamic droplet breakup," J. Fluid Mech. 940, A17 (2022).

 49S.-G. Kim and W. Kim, "Drop impact on a fiber," Phys. Fluids 28, 042001 (2016)
- ⁵⁰G. Liang and I. Mudawar, "Review of mass and momentum interactions during drop impact on a liquid film," Int. J. Heat Mass Transfer 101, 577 (2016).
- ⁵¹C. Clanet, C. Béguin, D. Richard, and D. Quéré, "Maximal deformation of an impacting drop," J. Fluid Mech. **517**, 199–208 (2004).
- 52F. Bierbrauer, N. Kapur, and M. C. T. Wilson, "Drop pinch-off for discrete flows from a capillary," ESAIM: Proc. 40, 16 (2013).
- ⁵³D. Broboana, A.-M. Bratu, I. Magos, C. Patrascu, and C. Balan, "Kinematics of the viscous filament during the droplet breakup in air," Sci. Rep. 12, 1774 (2022).
- ⁵⁴I. V. Roisman, A. Lembach, and C. Tropea, "Drop splashing induced by target roughness and porosity: The size plays no role," Adv. Colloid Interface Sci. 222, 615 (2015)
- ⁵⁵L. Deng and S.-C. Zhao, "Disintegration behavior of droplets impacting hydrophilic fibers," Langmuir 41, 13357 (2025).